

An atoms-to-mesoscale approach to ice-vapor surface dynamics with a quasi-liquid interface

Steven Neshyba¹, Tia Böttger¹, Rohan Crossland¹, Spencer Racca-Gwozdzik¹, Ella Slattery¹, Maximilian Bloom, Noah Zimmer¹, Penny M. Rowe², and Jacob Price¹

¹University of Puget Sound, Tacoma Washington USA

²North West Research Association, Redmond Washington, USA

Abstract

We explore the hypothesis that a key factor in determining the dynamics and morphology of faceted ice-vapor surfaces is the quasi-liquid layer that forms at this interface at temperatures above 240 K. We do so by modeling the ice surface as a system of reaction-diffusion equations in which the time scales of quasi-liquid freezing and melting, horizontal diffusion, and exchanges with the vapor phase are made explicit. Model parameterizations are informed by atomistic (molecular dynamics) simulations, mesoscale simulations of the vapor field around growing and ablating ice crystals, and quantitative ice surface morphologies derived from scanning electron microscope experiments. The outcome is a more unified, predictive, and experimentally grounded picture of the dynamics and morphology of faceted ice-vapor surfaces than has previously been presented.

Plain Language Summary

This is a mathematical exploration of the texture of ice surfaces on a microscopic scale. The main hypothesis is that this texture is governed by the behavior of a thin layer of water, intermediate between ice and liquid, that is known to form at the ice-air interface. We carry out this exploration by constructing a set of mathematical relationships that, when solved on a computer, reveal how parts of this quasi-liquid layer migrate to other regions of the ice surface, freeze, or evaporate into the air. The form and parameters of these equations are informed by insights from images of ice surfaces from scanning electron microscope experiments, and molecular-level modeling. We believe the insights obtained from this effort will be useful not only from a fundamental perspective, but also practically, especially in connection to the role of ice clouds in Earth's climate system.

1. Introduction

Why we care about ice crystal morphology ... the crystals that make up cirrus clouds modulate Earth's climate by reflecting or scattering sunlight before it reaches Earth's surface, but the extent to which they do that depends on the morphology of those crystals. Hexagonal prisms dominate, but there are lots of variations on that theme: long and thin hexagonal needles, short and wide plates, sometimes indented at the ends, or hollowed, or even dendritic forms, like snowflakes. Their surfaces can be smooth or rough on a scale that matters to light of comparable wavelength (Järvinen et al. 2023).

Numerous models of ice surface morphology and dynamics during vapor depositional growth have been presented. Harrington and Pokrifka (2021) provide an excellent review. Of these, models rooted in atomistic structure and processes are appealing because of the evident connection between molecular structure on the one hand, and high-resolution microscopic observations (such as scanning electron microscopy) on the other; a familiar example is that crystals of water ice are understood to owe their hexagonal shape to the hexagonal structure of the unit cell of an ice lattice. Molecular Dynamics studies have contributed greatly to this effort (see, e.g., (Llombart, Noya, and MacDowell 2020))

Of particular interest here is the Burton-Cabrera-Frank theory of crystal growth, also called classical nucleation theory, or CNT. CNT's atomistic view of the process of crystal growth goes along the following lines: when a gas-phase molecule (e.g., a water molecule) encounters a crystalline surface, it initially becomes attached to that surface as an "admolecule." Not yet part of the crystal's lattice, this admolecule diffuses across the surface until it meets one of two fates: either it fills an unoccupied position in the crystal lattice (often visualized as a step between ledges), or else it detaches from the surface and re-enters the gas phase. New layer formation is governed by a 2D nucleation process in which the step free energy plays a crucial role (Kuroda and Lacmann 1982).

CNT has long framed how we think about ice crystal growth from the vapor phase, but it is not reliable when it comes to describing the behavior of crystals placed in an inhomogeneous vapor field on a mesoscopic scale. To be specific, when a growing faceted ice crystal is situated in a supersaturated vapor field, it is easy to show that the surrounding water vapor concentration will be drawn down in such a way that facet intersections (i.e., crystal corners) will experience persistently higher vapor pressures than facet centers. CNT predicts that this would result in faster growth at those corners, leading ultimately to dendritic forms (e.g., snowflakes). However, under typical cirrus cloud conditions, it is known that hexagonal prisms resist that tendency, and instead maintain their faceted, hexagonal form.

An analogous circumstance arises when faceted crystals are situated in a subsaturated vapor field, in which case water vapor ablated from the surface distributes itself in such a way that crystal corners experience persistently *lower* vapor pressure compared to facet centers. CNT predicts that this would result in faster ablation at facet corners, eventually leading to a rounded crystal geometry. But our laboratory studies show that under such circumstances crystals typically maintain their faceted shape (albeit roughened on a micrometer scale), despite lower vapor conditions at corners.

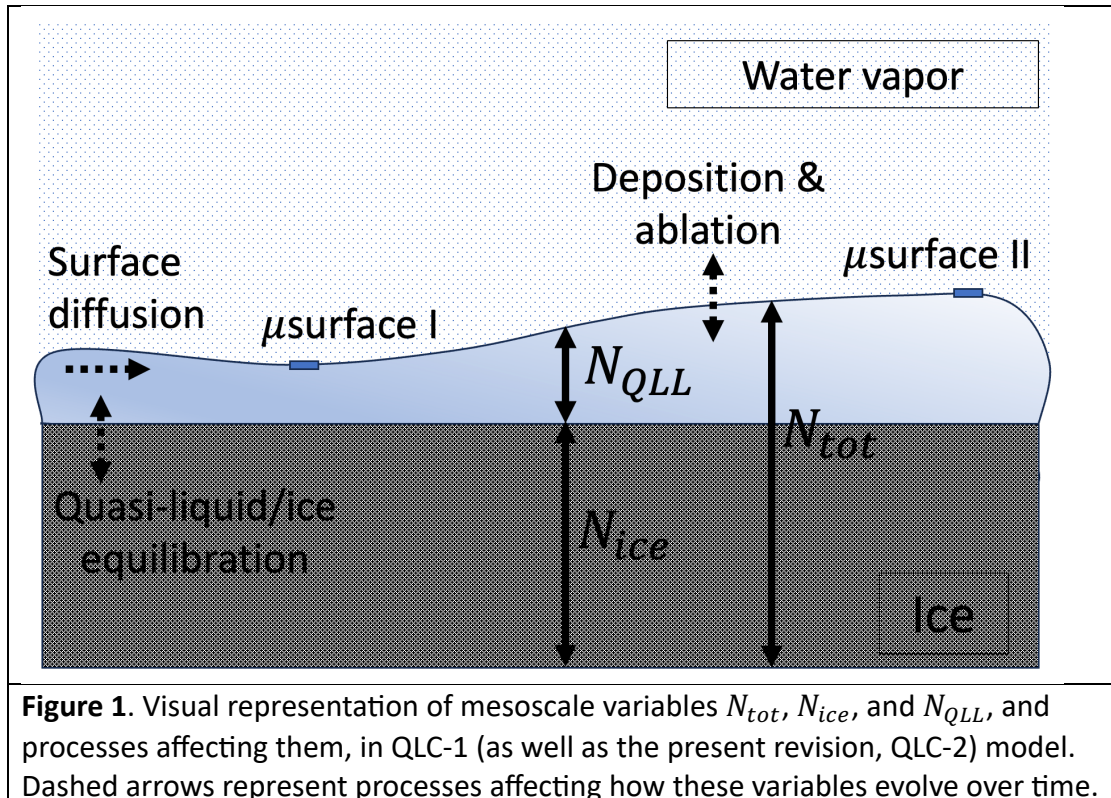
Both cases just described can be summed up as a resilience of hexagonal prismatic faceting despite persistent inhomogeneities in the overlying vapor field. Classical nucleation theory has no satisfactory explanation for this resilience. (However, see Jayaprakash et al (1983)).

To add to that criticism is the lack of fealty of CNT to what is known about the molecular structure of the ice-vapor interface. When the temperature of ice rises above 240 K, both experiment and theoretical studies have shown that the interface is entirely covered by a quasi-

liquid layer (QLL); molecular dynamics studies have shown that water molecule striking the surface are thermalized by the QLL efficiently and quickly (on a picosecond time scale) (Neshyba et al. 2009). On the other hand, recent experimental work has shown that there really are steps and ledges *underneath* the QLL, i.e., at the interface between the QLL and the underlying ice (Murata, Nagashima, and Sazaki 2019).

Bridging the gap between atomistic and mesoscale levels, therefore, would seem to require an atomistic model that begins with the existence of a QLL (above 240 K), that preserves relevant parts of CNT as much as possible. One such attempt was presented by some of the authors in 2016 (Neshyba et al. 2016) (henceforth N2016), in the form of a dynamic quasi-liquid continuum model, referred to here as QLC-1. Because that model forms the foundation of the revision presented here (“QLC-2”), we summarize it next.

QLC-1 frames the problem of ice surface dynamics in terms of two mesoscale variables, N_{tot} and N_{QLL} , which represent the thickness of the ice surface and its quasi-liquid part, respectively, at each point on the surface (see Fig. 1). Time evolution of these variables is governed by a pair of reaction-diffusion equations that represent the three processes indicated in Fig. 1, namely, (i) exchanges (deposition and ablation) of QLL molecules with the vapor phase, (ii) horizontal diffusion of QLL molecules across the ice surface, and (iii) interconversion of QLL molecules to/from the underlying ice.



The main insight afforded by QLC-1 is that it provides a mechanism by which faceted ice crystal growth can occur. At the heart of that mechanism is a process N2016 termed “diffusive slowdown,” which can be summarized as follows:

- 1) At the micrometer level, the QLL can be thought of as consisting of a continuum of microstates, ranging from a thin, less-volatile microstate labeled μ surface I, to a thick, more-volatile one labeled μ surface II. The difference in these volatilities is quantified in QLC-1 as a difference in equilibrium supersaturation, σ^0 . Evidence for the existence of these microstates, and their difference in volatility, has emerged mainly from molecular dynamics simulations (N2016).
- 2) In a growing ice crystal, each time a new layer forms, a new pair of these microstates appears on the surface. Designating the horizontal distance between new layers and their predecessors as “ λ ” (see Fig. 2), we see that $\lambda_{corner} < \lambda_{center}$; this is because new layers typically form at facet corners, where the water vapor concentration is highest.

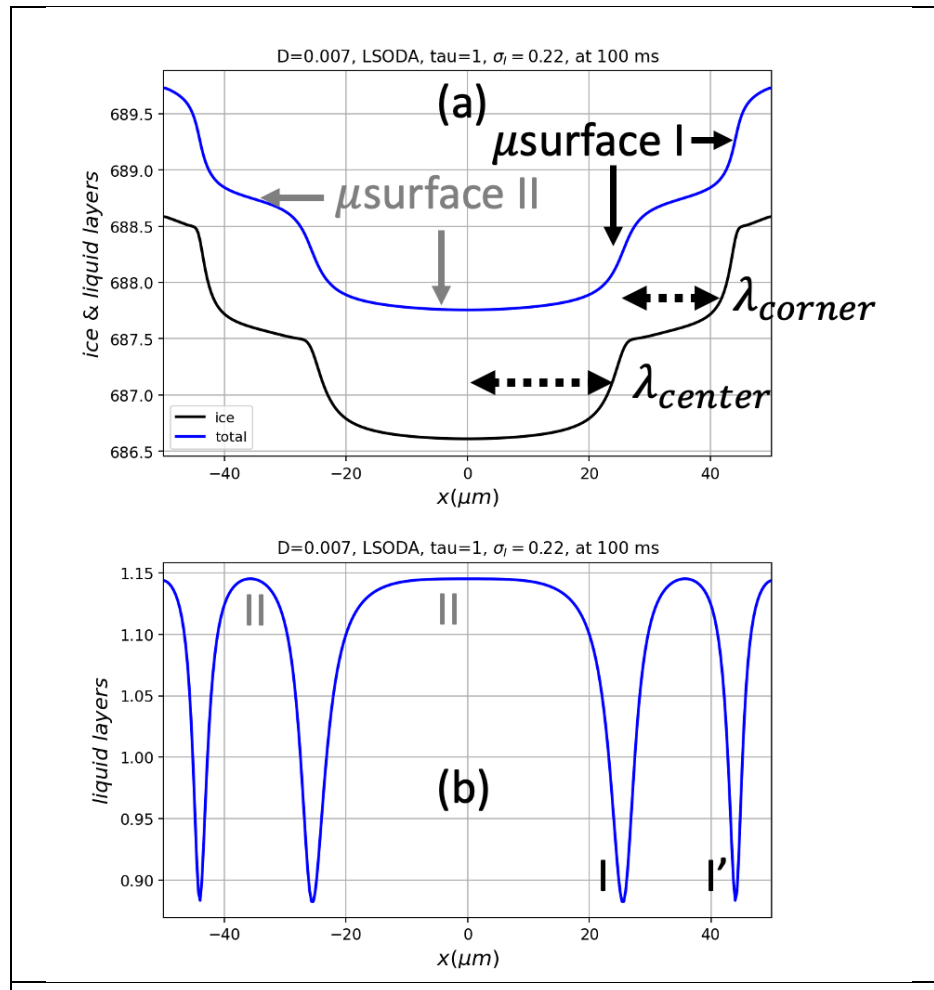


Figure 2. An ice surface covered by QLL, as simulated by QLM-2.

- 3) Horizontal diffusion moves quasi-liquid away from thicker, μ surface II-like regions of the surface, and toward thinner, μ surface I-like regions. However, because μ surface I accounts for a smaller fraction of the total surface area (as seen in Fig. 2(b)), diffusion has a greater proportional effect on it. As a consequence, diffusion leads to an increase in the average volatility of the surface, causing the surface as a whole to experience a net “diffusive slowdown” in its growth rate. (The reader is referred to N2016 for a quantitative version of this argument.)

A second process identified in N2016 is that diffusive slowdown is not homogeneous across a facet. Instead, in a growing ice crystal, more diffusive slowdown occurs at facet corners. The reason is as follows:

- 4) In regions where λ is small, QLL thickness gradients are large. In Fig. 2(b), for example, it is clear that the gradient in QLL thickness at I' is greater than at I . It follows that, in a growing ice crystal, more diffusive slowdown occurs at facet corners.

Limit cycles as an explanation for steady-state growth of ice facets.

In summary, a flat facet exposed to supersaturated vapor will initially experience higher growth rates at its corners, because of higher vapor concentration there. That leads to a higher step density (smaller λ) at facet, hence a reduction in the growth rate at corners relative to facet centers. When these effects become balanced – which can (and does) occur as an emergent property of the equations of motion defining QLC-1 (and QLC-2, as we will show here), the result is equal growth rates across the entire facet. That steady-state condition, known in nonlinear dynamics as a limit cycle, is interpreted at the mesoscale (e.g., in a high-resolution optical or scanning electron microscopy experiments) as faceted growth.

QLC-1 suffered from some structural deficiencies, however, of which the most important for our present purpose is that the time scale of process (iii) illustrated in Fig. 1, the interconversion of quasi-liquid and ice, was fixed relative to processes (i) and (ii). In real crystal facets, these time scales are expected to vary from facet to facet, or as a function of temperature and vapor pressure. These time scales should therefore be adjustable quantities within the theory.

Our goal in this communication is to evaluate strengths and weaknesses of a revised quasiliquid continuum model for ice crystal growth and ablation designed to address this deficiency. Section 2 presents such a model, referred to here as QLC-2. Section 3 presents key insights from recent scanning electron microscopy experiments, followed by Section 4, which presents QLC-2 results relevant to those insights. Section 5 discusses implications of these results in other contexts, including cirrus ice crystal morphologies and ideas from nonlinear dynamics, especially the stability of limit cycles of reaction-diffusion systems such as QLC-2.

2. A revised Quasi-liquid Continuum model (QLC-2)

Like QLC-1, QLC-2 represents an ice surface as two mesoscale variables and three processes, as shown in Fig. 1. The governing equations are

$$\frac{dN_{tot}}{dt} = D_{QLL} \nabla^2 N_{QLL} + v_{kin} \sigma_m \quad (1a)$$

$$\frac{dN_{QLL}}{dt} = \frac{dN_{tot}}{dt} - (N_{QLL} - N_{QLL}^{eq}(N_{tot})) / \tau_{eq} \quad (1b)$$

Some notes about this model are as follows, with differences between it and QLC-1 noted:

- 1) $D_{QLL} \nabla^2 N_{QLL}$ represents surface diffusion of the QLL; the underlying ice is considered immobile on time scales considered here.
- 2) v_{kin} is the rate at which vapor-phase water molecules strike the quasi-liquid; it is assumed that these stick with 100% efficiency, and thermalize on a picosecond time scale (i.e., instantaneously within the time scales of a QLC-2 simulation).
- 3) $N_{QLL}^{eq}(N_{tot})$ prescribes the thickness of quasi-liquid when it is in equilibrium with the underlying ice, according to

$$N_{QLL}^{eq}(N_{tot}) = \bar{N} - N^* \sin(2\pi N_{tot}) \quad (2)$$

This formulation ensures that the QLL thickness varies continuously from the thin microstate ("μsurface I") with thickness $\bar{N} - N^*$, to the thick microstate ("μsurface II") with thickness $\bar{N} + N^*$. (Note the connection to work of (Benet et al. 2019, Eq. 8), that also shows a sinusoidal dependence.)

- 4) Because μsurfaces I and II have different volatilities, the surface supersaturation at a given point on the surface (designated σ_m in Eq. 1a) is a function of both the microstate and the water vapor concentration above it. To compute σ_m , we define a variable m that quantifies the degree to which a given surface is similar to μsurface I or II,

$$m = \frac{N_{QLL} - (\bar{N} - N^*)}{2N^*} \quad (3)$$

With this definition, μsurface I will have $m = 0$, while μsurface II will have $m = 1$. We then express the surface supersaturation as

$$\sigma_m(x) = \sigma_I(x) - m\sigma^o \quad (4)$$

where σ^o is a measure of the difference in the equilibrium vapor pressure of μsurfaces I and II, and $\sigma_I(x)$ is the supersaturation relative to μsurface I, mentioned previously. We will assume here that both σ^o (a scalar quantity) and $\sigma_I(x)$ are fixed parameters of a given solution. Eq. 4 is at slight variance with, and simpler than, the corresponding expression in QLC-1.

- 5) Typically, a parabolic form is used to approximate $\sigma_I(x)$ appearing in Eq. 4,

$$\sigma_I(x) \approx \sigma_{I,corner} \times \left(c_r \left(\frac{x}{L} \right)^2 + (1 - c_r) \right) \quad (5)$$

where c_r is a “center reduction”, the fractional reduction of supersaturation at facet centers relative to facet corners,

$$c_r = 1 - \frac{\sigma_{I,middle}}{\sigma_{I,corner}} \quad (6)$$

Justification for this form is provided by simulations of the vapor field surrounding an ice crystal that is growing at a specified rate (see Section 3). Negative values of c_r are used to represent subsaturation conditions, when the ablating crystal produces higher water vapor concentration at facet centers, compared to facet corners.

- 6) τ_{eq} is a first-order relaxation constant describing the time scale at which quasi-liquid/ice equilibrium is achieved. That is, if we imagine a surface with quasi-liquid amount N_{QLL}^o , then equilibration after a time Δt occurs according to

$$N_{QLL}(t) = N_{QLL}^{eq}(N_{tot}) + \left(N_{QLL}^o - N_{QLL}^{eq}(N_{tot}) \right) e^{-\frac{\Delta t}{\tau_{eq}}} \quad (7)$$

If one takes the time derivative of Eq. 6, and assumes that Δt is small, the second term on the right-hand side of Eq. 1b results.

Equations 7 and 1b represent the primary departure of QLC-2 from QLC-1. With this revision, we are able to specify the rate of quasi-liquid/ice equilibration relative to processes (i) and (ii). Specifying a small value for τ_{eq} , for example, would represent the idea that quasi-liquid/ice equilibration is fast compared to those processes, while large τ_{eq} would mean the opposite. We do not have reliable observational values of τ_{eq} , but we do have a guidepost: because the “diffusive slowdown” mechanism for stabilization of faceted ice growth described above requires that quasi-liquid/ice equilibration be slow compared to surface diffusion, we should not be surprised if we find that large τ_{eq} leads to stable growth dynamics. We return to this topic below.

For the purpose of exploring solutions to the QLC-2 equations of motion, it is necessary to define values of the parameters appearing in Eqs. 1-7. To do so, we employ here two separate strategies. Common to both strategies are the following fixed values:

- \bar{N} and N^* , representing the difference in equilibrium number density between μ surfaces I and II (fixed at 1 and 0.143).
- σ^o , the amount by which the equilibrium vapor supersaturation of μ surface II exceeds that of μ surface I (fixed at 0.2).

- Δ_N , the thickness of a single layer of ice (fixed at 0.389 nm to approximate the thickness of a prismatic facet bilayer, as in N2016).

Within those constraints, it is useful to establish a physically realistic and self-consistent baseline scenario. A prominent example of self-consistency is the relationship between the surface diffusivity and the kinetic deposition rate (D and v_{kin}): both increase with increasing temperature. It is also the case that

Baseline strategy: Integrated QLC-2 combined with Vapor Field simulations

Here, we explicitly specify the following parameters:

- L , distance from facet center to corner.
- T and P_{amb} , temperature and pressure surrounding the crystal.
- $\sigma_{I,\infty}$, supersaturation of water vapor far from the crystal.
- τ_{eq} , the ice-QLL equilibration time constant.

Remaining parameters are then obtained by the following steps:

1. The surface diffusion coefficient is obtained from the ambient temperature,

$$D = D^o \exp\left(-\frac{E_a}{R}\left(\frac{1}{T} - \frac{1}{T_o}\right)\right) \quad (8)$$

with $E_a = 22.8 \frac{kJ}{mol}$ and $D^o = 9.20 \times 10^{-4} \frac{\mu m^2}{\mu s}$ (based on a fit to diffusion data of (Price, Ide, and Arata 1999)).

2. The Hertz-Knudsen deposition speed is also temperature-dependent,

$$v_{kin} = P_{vap}^{eq}(T) \times \left(\frac{M_{H_2O}}{2\pi RT}\right)^{1/2} \quad (9)$$

where $P_{vap}^{eq}(T)$ is water's equilibrium vapor pressure, and M_{H_2O} is its molar mass.

3. Vapor Field simulations may be used to define properties of P_{vap} in the air space surrounding growing and ablating ice crystals. Details about these simulations are given in Appendix 1, the main point to emphasize here is that those simulations produce profiles of water vapor supersaturation along a faceted surface, $\sigma_I(x)$, that are well-approximated by the parabolic form for $\sigma_I(x)$ given in Eq. 5. The Vapor Field simulations yield values σ_I at key locations, such as at the corners and centers of facet. Those values, in turn provide a means of parameterizing c_r for use in Eq. 5, namely,

$$c_r(\%) \equiv \frac{\sigma_I(\text{corner}) - \sigma_I(\text{center})}{\sigma_I(\text{corner})} \times 100 \quad (10)$$

4. g_{ice} , the growth rate of the ice surface, is obtained iteratively, as follows:

- i. A Vapor Field simulation takes growth rate of the ice surface (g_{ice}) as an input, along with L , T , P_{amb} , and $\sigma_{I,\infty}$, and predicts $\sigma_{I,corner}$ and c_r .
- ii. A QLC-2 simulation takes $\sigma_{I,corner}$ and c_r as inputs, along with L , T , P_{amb} , and $\sigma_{I,\infty}$, and predicts a new growth rate of the ice surface (g'_{ice}).
- iii. These steps are repeated until g_{ice} and g'_{ice} agree within some tolerance level.

Once we have a set of “baseline” parameters in this way, we explore variations on that baseline by explicitly varying the inputs

- L , the distance from facet center to corner.
- D , the surface diffusion coefficient
- v_{kin} , the Hertz-Knudsen deposition velocity
- τ_{eq} , the ice-QLL equilibration time constant.
- $\sigma_{I,corner}$ and c_r , which describe a parabolic representation of $\sigma_I(x)$.

3. Results from QLC-2 simulations

Here we describe the results QLC-2 simulations, focusing on curvature of growing faceted surfaces (and hence the implied horizontal distance between adjacent ice layers, described above as “ λ ”), and a comparison of facet curvature under growth vs ablation conditions.

Figure 3 shows a modeled ice crystal surface under growing and ablating conditions. The growth scenario on the left of the figure resulted from supersaturated water vapor concentrations, distributed as shown in Fig. 3(a). Figures 3(b) and 3(c) show that these conditions lead to steady state, “V”-shaped profiles, in which the surface is dominated by primarily μ surface I – like microstates. This scenario exhibits more tightly bunched (smaller λ) at facet boundaries, which in turn (as described above in the summary of diffusive slowdown) leads to a net increase in volatility of the surface as a whole, hence faceted growth.

The ablating scenario on the right of Fig. 3 resulted from subsaturated water vapor amounts, distributed as shown in Fig. 3(d). Figures 3(e) and 3(f) show that these conditions also lead to steady state, although in this case the profile is “ Λ ” shaped (i.e., rounded), the surface is dominated by μ surface I – like microstates, and the layer bunching leads to *reduced* volatility of the surface near the corners, hence faceted ablation.

The model results shown in Fig. 3 also suggest the following general pattern: growing ice facets possesses convex curvature, whereas ablating ice facets possess concave curvature. A useful metric for describing the curvature of steady state profiles such as those appearing in Fig. 3 is the local slope of the surface. Here we quantify that slope as a mean horizontal distance between successive molecular layers, defined as

$$\bar{\lambda} = L/n_{steps} \quad (11)$$

For example, both facet profiles in Fig. 3 are characterized by $\bar{\lambda} \approx 1 \mu\text{m}$.

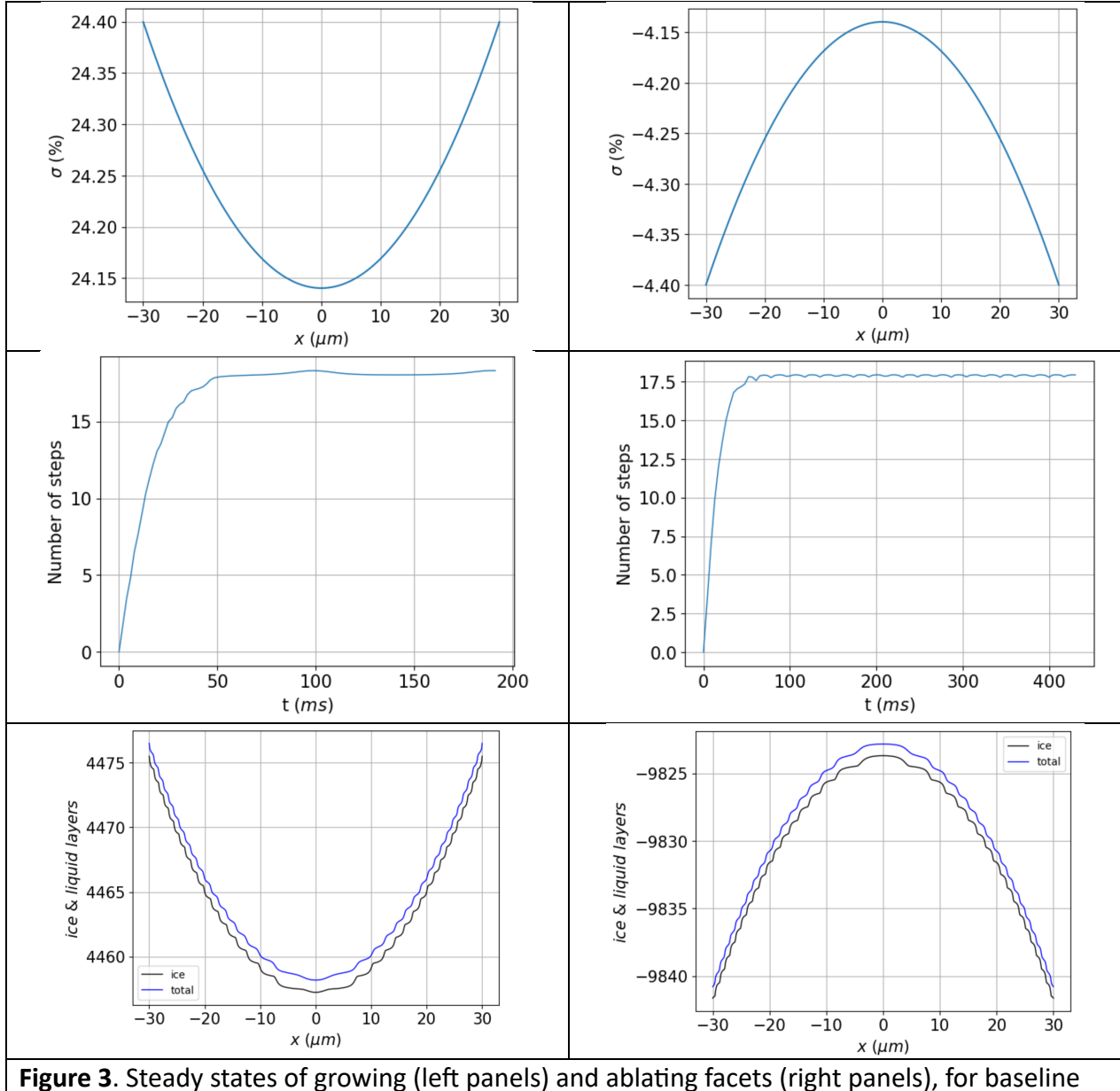


Figure 3. Steady states of growing (left panels) and ablating facets (right panels), for baseline parameters constructed according to Strategy B (see Table 1). Top: vapor supersaturation adjacent to a facet spanning $60 \mu\text{m}$; Middle: time evolution of the number of steps, beginning with a flat surface ($\# \text{steps} = 0$) to steady state; Bottom: steady-state profiles of QLL-covered faceted ice surfaces.

Figure 4 shows the dependence of the mean horizontal layer separation, $\bar{\lambda}$ (introduced above), on the parameter z , defined by

$$z \equiv \left(\frac{D}{c_r v_{kin}} \right)^{\frac{1}{2}} \quad (12)$$

where (as described above) D is the surface diffusion coefficient, L is the edge length of the crystal, and v_{kin} is the kinetic deposition velocity. In constructing Fig. 4, we began with self-consistent set of parameterizations for the baseline scenario, but for all other points freely assuming a range of values of D , c_r , and v_{kin} , as indicated in the caption.

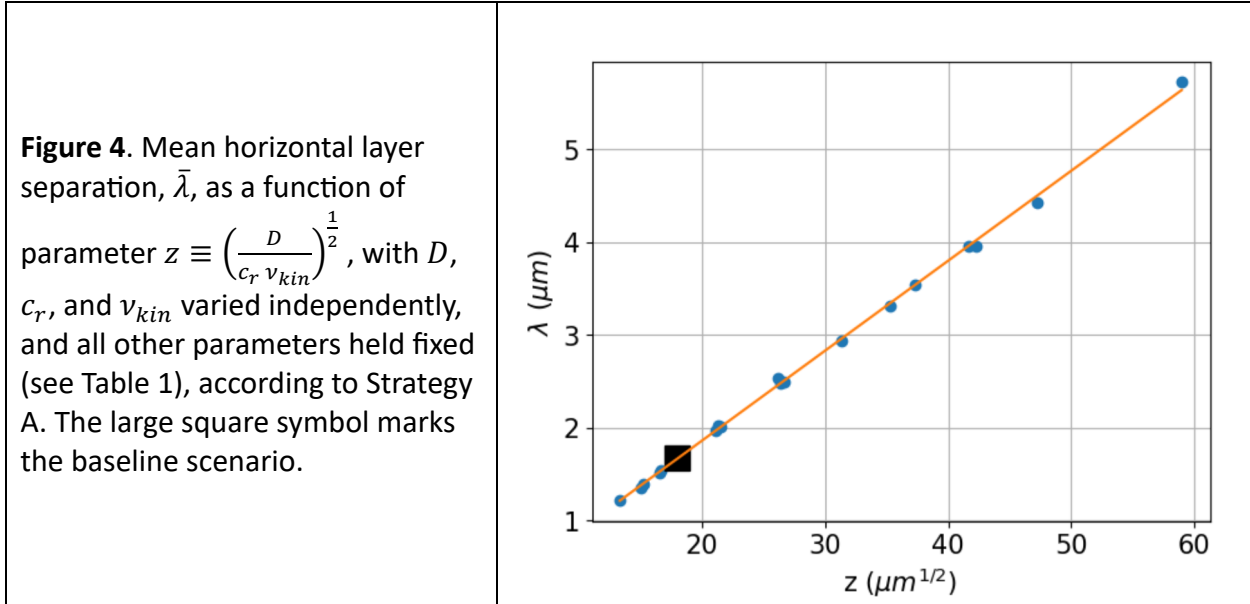


Figure 4 shows that a good parameterization is a straight line,

$$\bar{\lambda}_g = m_g z + b_g \approx m_g z \quad (13a)$$

with best-fit parameters $m_g = 0.0970 \mu\text{m}^{1/2}$, $b_g = -0.0793 \mu\text{m}$. The approximation is due to the fact that b_g is small. Best Analysis of ablating scenarios also yields a straight line,

$$\bar{\lambda}_a = m_a z + b_a \approx m_a z \quad (13b)$$

with slightly different parameters: $m_a = \dots \mu\text{m}^{1/2}$ and $b_a = \dots \mu\text{m}$.

Figure 5 shows values of $\bar{\lambda}$ for a range of corner supersaturations ($\sigma_{I,corner}$), holding parameter z constant. We see that when conditions begin to become supersaturated, $\bar{\lambda}_g$ starts off at about $2 \mu\text{m}$ and declines monotonically at high supersaturations. On the left-hand side are shown results when conditions are subsaturated. We see that under these conditions, $\bar{\lambda}_a$ declines monotonically away from zero subsaturation.

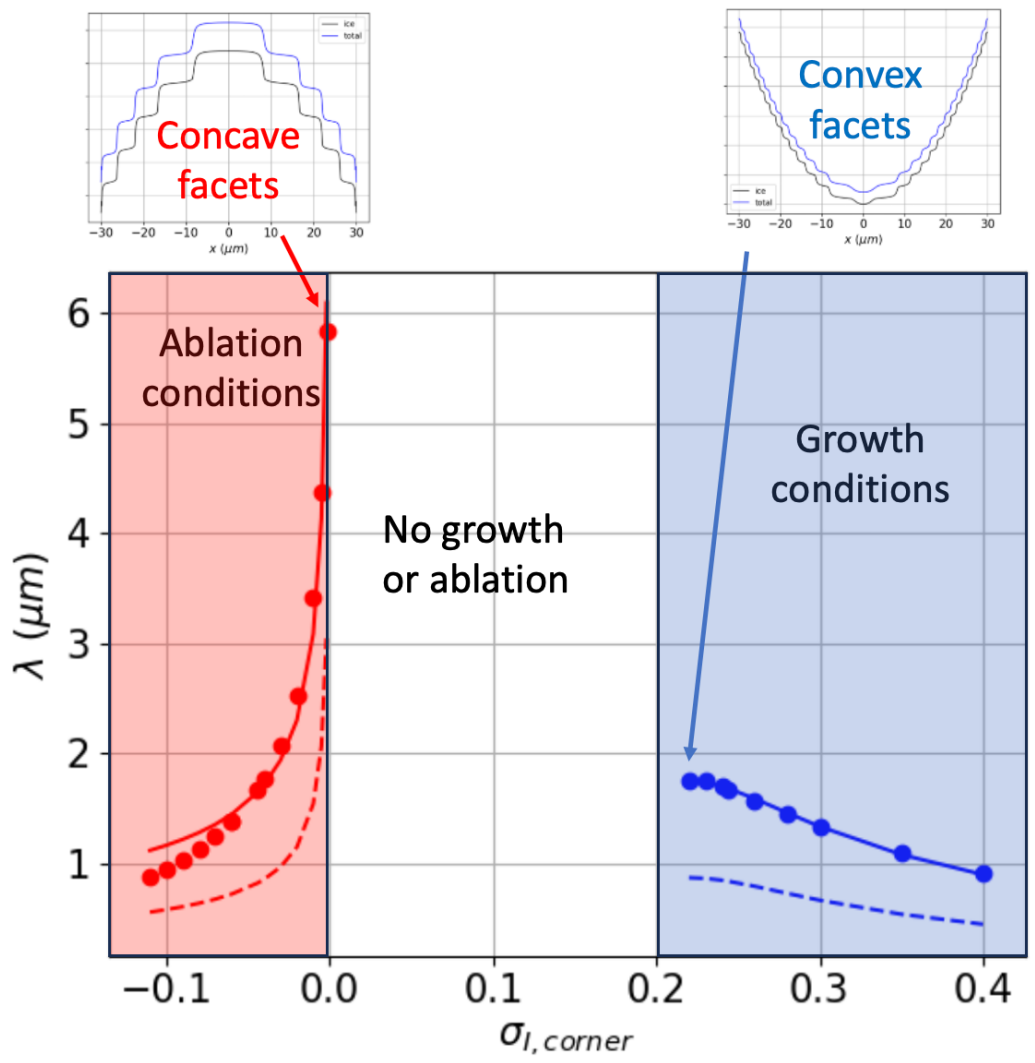


Figure 5. Mean horizontal layer separation ($\bar{\lambda}$) as a function of corner supersaturation σ_{corner} . Solid lines show best-fit approximations according to Eqs. 14a and 14b with $\frac{z}{z_{ref}} = 1$, dashed lines with $\frac{z}{z_{ref}} = \frac{1}{2}$.

Figure 5 also shows the results of applying a factorized mathematical expression that combines the observation that $\bar{\lambda}$ depends linearly on parameter z , but nonlinearly on $\sigma_{I,corner}$. For growth conditions, we find that an exponential nonlinear dependence on $\sigma_{I,corner}$ works well,

$$\bar{\lambda}_g \approx \bar{\lambda}_{g,o} \times \frac{z}{z_{ref}} \times \left(1 - \exp \left(-\frac{1}{(\sigma_{I,corner} - \sigma_o)x_{g,o}} \right) \right) \quad (14a)$$

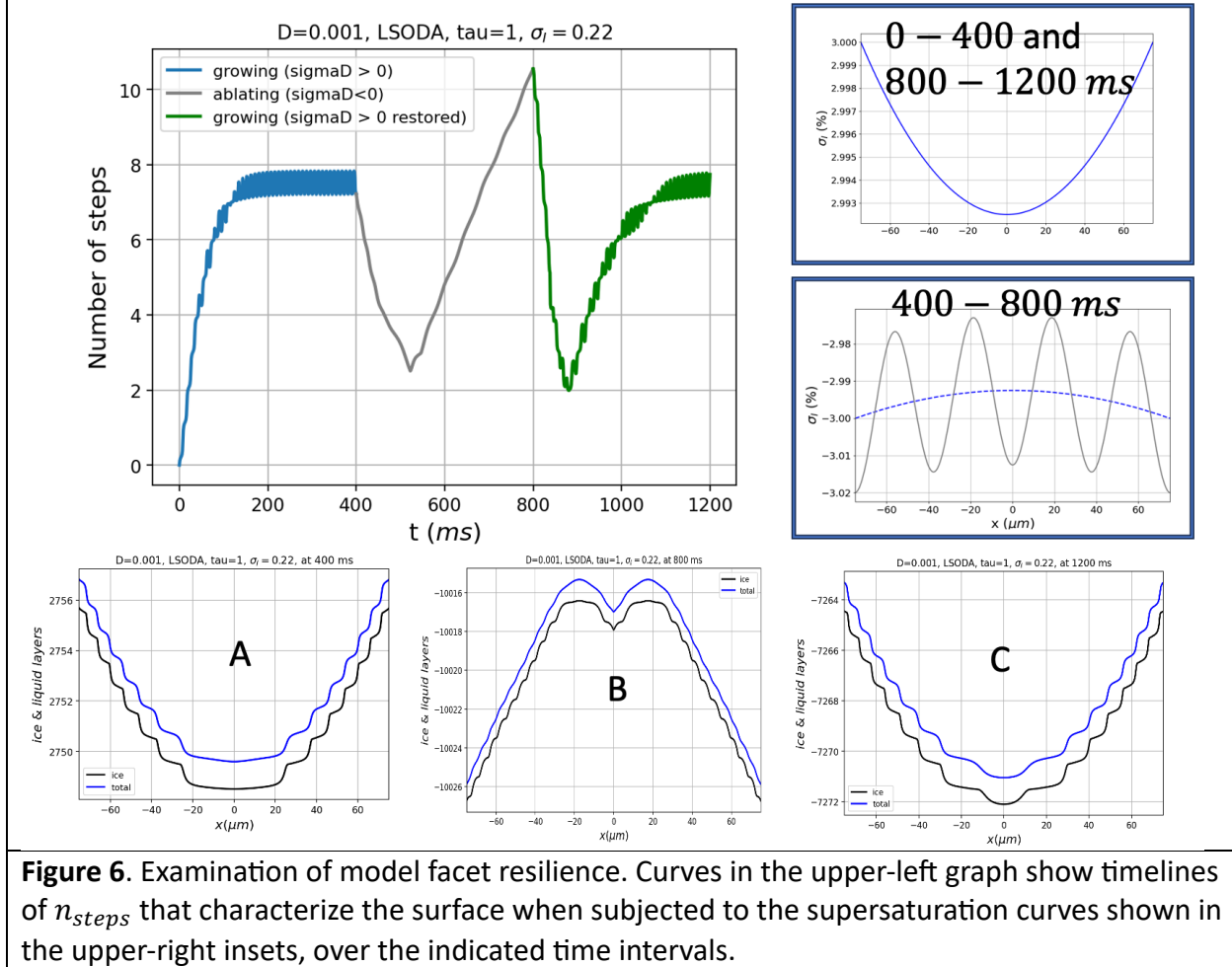
while for ablating facets, we use a power dependence on $\sigma_{I,corner}$,

$$\bar{\lambda}_a \approx \bar{\lambda}_{a,o} \times \frac{z}{z_{ref}} / (\sigma_{I,corner})^{x_{a,o}} \quad (14b)$$

Using best-fit parameters $\bar{\lambda}_{g,o} = 2.050 \mu m$, $x_{g,o} = 6.68$, $\bar{\lambda}_{a,o} = 0.535 \mu m$, $x_{a,o} = 0.417$, we show in Fig. 5 the results of these expressions. The fit is very good for ablation conditions as $\sigma_{I,corner}$ approaches zero, although it overestimates $\bar{\lambda}_a$ at larger subsaturations.

Lastly, we investigate the resilience of steady-state solutions to perturbations. The sequence of images in Fig. 6 begins with an initially-flat profile, which is then subjected to the following sequence:

1. From 0 to 400 ms, the surface is been exposed to the supersaturated water vapor curve shown in the inset located in the upper right part of the figure. By 400 ms, the profile has evolved to the faceted, steady-state profile labeled "A".
2. From 400 to 800 ms, a perturbation is introduced in the form of the subsaturated water vapor curve shown in the inset located in the middle-right part of the figure. During this time, the surface evolves into the highly perturbed state labeled "B".
3. From 800 to 1200 ms, the initial supersaturated water vapor regime is restored. During this time, the surface recovers its pre-perturbation faceted profile labeled "C".



Conclusion ... qualitatively, QLC-2 exhibits resilience.

4. Results of ESEM/GNBF retrievals

Environmental SEM of imaging of ice crystals has seen considerable development in recent years, including the ability to image actively growing and ablating crystals by manipulating the temperature and pressure inside an SEM chamber (Pfalzgraff, Hulscher, and Neshyba 2010; Zimmermann et al. 2007). In tandem with those developments are computer codes for generating quantitative surface morphologies using a Gauss-Newton in a Bayesian Framework (GNBF) algorithm (Butterfield et al. 2017). The combination – a process we will refer to here as “ESEM/GNBF retrieval” – provides opportunities for vetting model predictions of surface morphology against experiment at resolutions that are not quite commensurate with one another, but approaching that level (see details in Appendix 1).

Here we consider two questions focused on using QLC-2, namely, the curvature of growing faceted surfaces (and hence the implied horizontal distance between adjacent ice layers, described above as “ λ ”), and a comparison of facet curvature under growth vs ablation conditions.

Considering first the curvature of growing faceted surfaces, the left-hand panels of Figure 6 display ESEM images of three ice crystals observed under growing conditions. The right-hand panels display ESEM/GNBF retrievals of the surfaces highlighted in each.

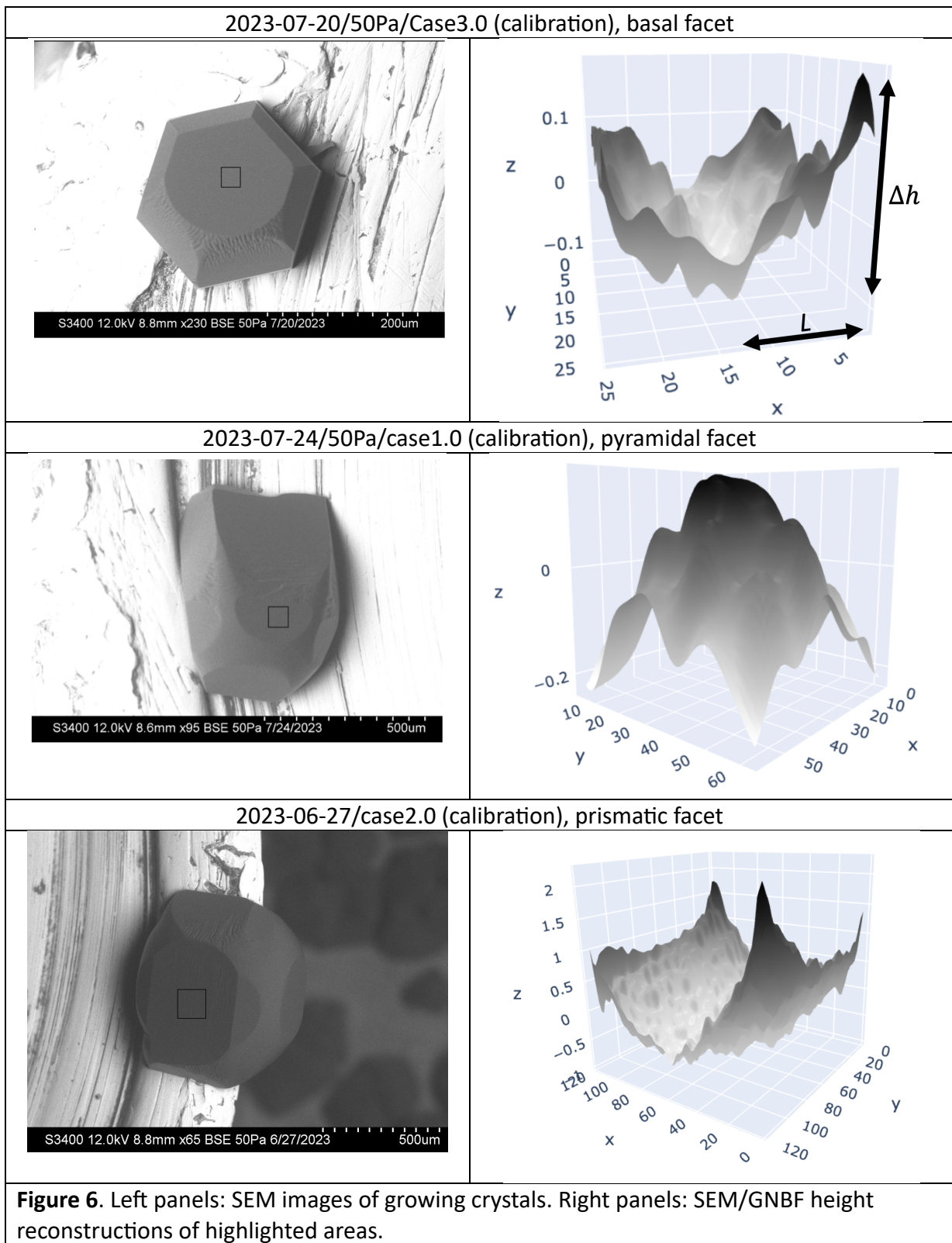
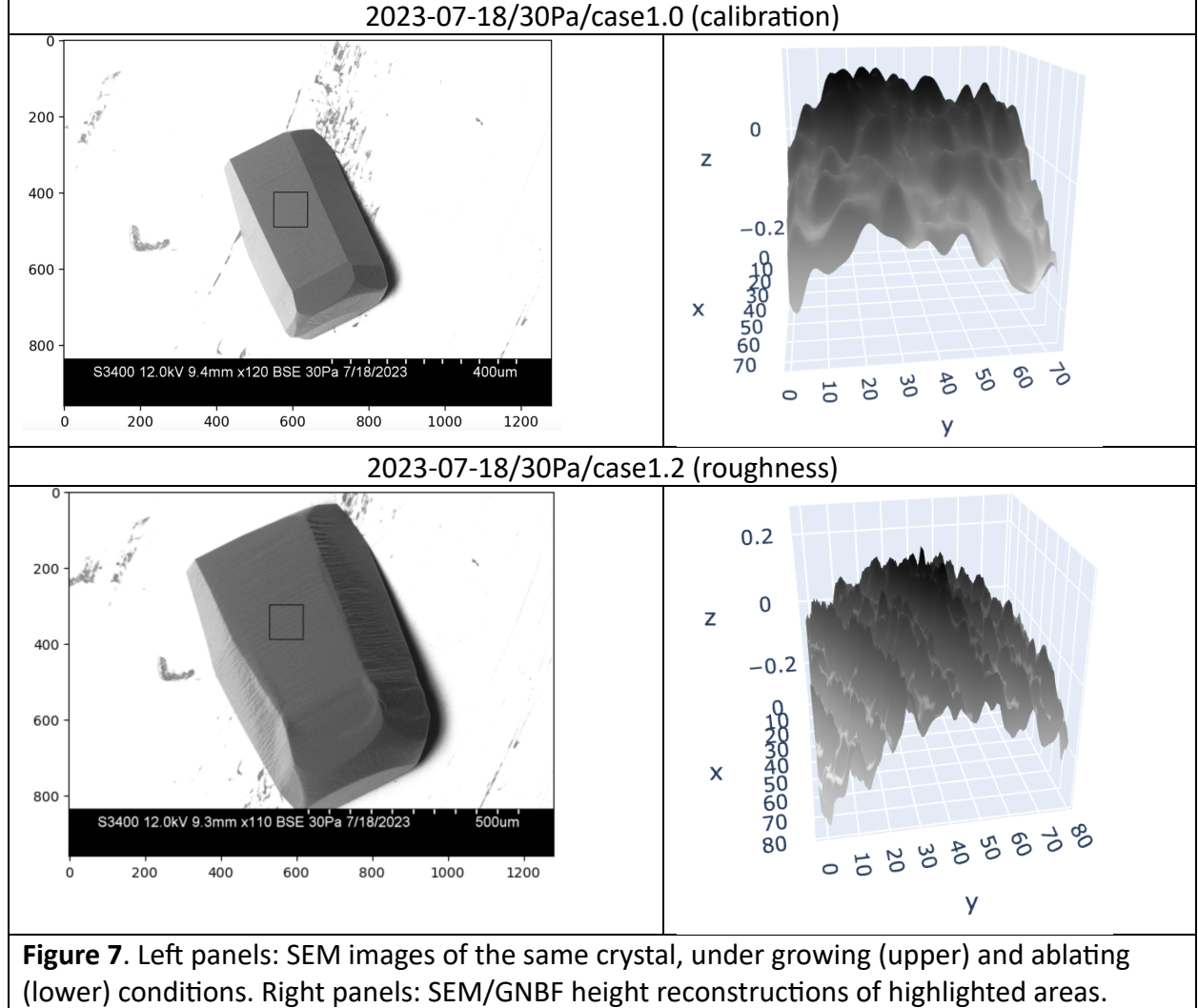


Figure 7 displays ESEM images of a single ice crystal observed under growing and ablating conditions. In both cases, the images on the left-hand-side of the figure show that facets are identifiable. That is, faceted *ablation* occurs, as well as (the expected) faceted growth – even when the surface is quite rough.



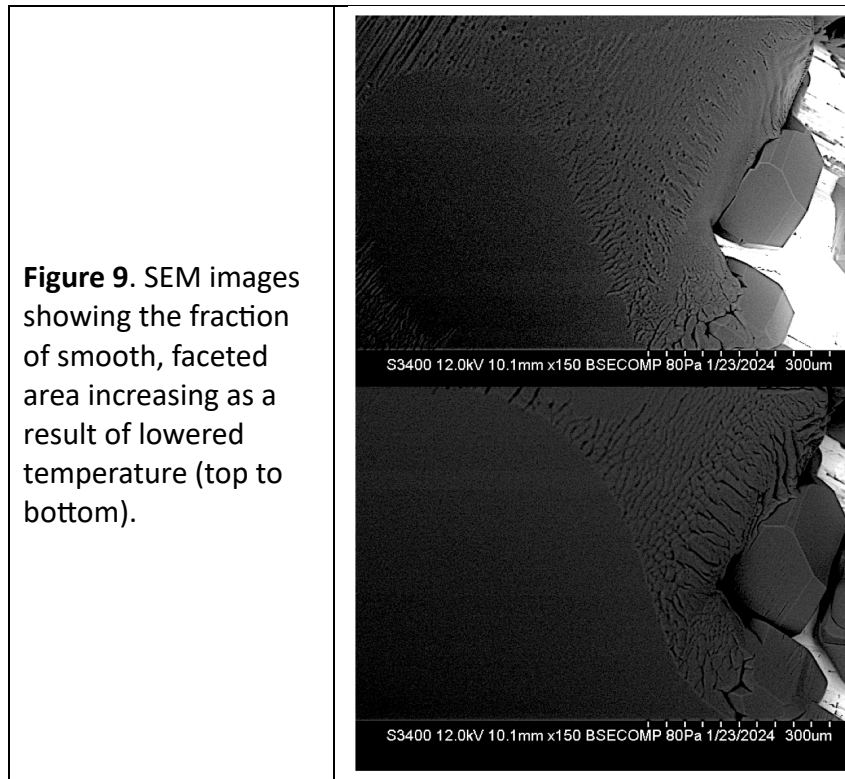
The horizontal spacing between successive layers of ice are computed from these images using

$$\lambda_{SEM} \approx \frac{\Delta h_l L}{\Delta h} \quad (11)$$

where L and Δh are defined in Fig. 3, and Δh_l is the thickness of a single layer of ice; we take the latter to be $\Delta h_l \approx 0.4 \text{ nm}$ to represent all three facets, which is good to one significant figure. We find that $\lambda_{SEM} \approx 0.02 - 0.2 \mu\text{m}$ in all instances appearing in Figs. 6 and 7.

In ESEM experiments, facets exhibit a certain resilience, in that an initially faceted surface, after it is roughened by some perturbation, can usually be restored to its initial smooth faceted state

after the initial conditions are restored. An example is shown in Fig. 9, in which the fraction of smooth, faceted area is seen to increase as a result of lowered temperature.



What resilience, if any, is exhibited by modeled facets? Figure 10 is an examination of this question.

5. Summary and discussion

The QLC-2 model presented here offers significant technical improvements over the QLC-1 model reported in N2016, in that its numerical solutions are more stable, and its parameterizations are better constrained by independent numerical simulations of the overlying vapor field, i.e., the dependence of the center reduction parameter (c_r) on crystal size (L).

More fundamentally, QLC-2's equations of motion embody a more faithful atomistic representation of ice/QLL freeze/melt equilibration. That connection, in turn, enables the theory to represent a more unified picture of ice surface dynamics than has previously been possible. The model predicts, for example, facet convexity and concavity under growth and ablation conditions (respectively), a pattern that is echoed in reconstructions of SEM-grown ice crystals. The model also provides a mechanism by which real ice crystals resist dendritic geometries when subjected to supersaturation conditions (i.e., faceted growth), and how they also resist rounding when subjected to subsaturation conditions (faceted ablation). It is, essentially, a theory of faceting that rests fundamentally on atomistic variations in the thickness and volatility of the quasi-liquid layer that are exposed as a crystal grows or ablates.

The model also predicts a certain resilience to perturbations – also echoed by real ice crystals – in that faceted surfaces that have been disrupted in some way recover when conditions favorable to faceting are restored.

QLC-2 makes an unexpected qualitative prediction about characteristic distances, quantified here as $\bar{\lambda}$, the mean distance between adjacent layers of ice. We find that $\bar{\lambda}$ separates mathematically as a product of two functions: one is a linear function of variable, $z \equiv \left(\frac{D}{c_r v_{kin}}\right)^{1/2}$, and the other is a highly nonlinear function of the surface supersaturation. We find that the latter is an asymmetrical function of the surface supersaturation, such that growth conditions lead to smaller values of $\bar{\lambda}$, while ablation conditions lead to larger values of $\bar{\lambda}$, for comparable departures from equilibrium. We have no ready explanation for this behavior, but we do note that SEM observations are consistent with these observations in the sense that ridges in rough facets of growing crystals are spaced more closely than in rough facets of ablating crystals. As noted previously, this coincidence is subject to a very big caveat, namely, that the depths of these characteristic distances are vastly different in QLC-2 compared to experiment: in the former it is a few monolayers, while in the latter it is thousands of monolayers.

Qualitative implications of this work for cirrus cloud particles can be summarized as follows: As such particles fall through Earth's atmosphere, such crystals will encounter increased pressure, hence smaller D_{vap} , but also increased temperatures (unless there is an atmospheric inversion), hence larger D_{vap} . When the effect of increased pressure dominates, QLC-2 predicts enhanced growth at facet corners, hence greater facet convexity, and therefore a greater propensity toward hollowed crystal structures. When the effect of increased temperature dominates, however, we can expect more regular hexagonal shapes. Although there is no single observational datum that would help us resolve these predictions, we can comment that in exceptionally cold regions (such as the Antarctic Plateau), or even in mid-latitudes where high-altitude cryo-capture of ice crystals on ground-launched balloons is possible, observations have shown that cirrus clouds are frequently hollowed, suggesting dominance of increased pressure distinctive (Magee et al. 2014, 2021; Walden, Warren, and Tuttle 2003).

We should note that the results presented here do not consider variations in parameters σ^o , N^* and \bar{N} , because these values are highly uncertain; more detailed molecular dynamics calculations could provide plausible values, but those studies have not been reported. We can speculate that because different facet types (basal, prismatic, or pyramidal) have distinct underlying crystal cell structures, their quasi-liquid properties will also be Exploratory numerical studies varying the thickness of a single “layer” of ice has shown that a proportional increase in $\bar{\lambda}$ results. Preliminary numerical experiments varying N^* and \bar{N} have shown that ...

A separate speculation concerns the observation that the $D^{1/2}$ dependence of $\bar{\lambda}$ values exhibited by QLC-2 is the same as in Turing patterns. In one sense this should come as no surprise, since Turing's theory, like QLC-2, is based on a reaction-diffusion equation. But there

are also very big differences, including the fact that Turing's analysis proceeds from an analysis of sensitivity to perturbations to an initially homogeneous distribution of chemical species, whereas the patterns in QLC-2 emerge as steady states of the equations of motion.

Finally, we note that the atoms-to-mesoscale approach represented in QLC-2 is not as fully integrated as we would like it to be ... maybe some insight from Jake's heterogeneous multiscale approach is the way forward on this (Shohet et al. 2020).

Appendix 1 – Vapor field code

Simulation of the water vapor partial pressure, $P_{vap}(x, y)$, in the space surrounding a square-shaped crystal shown in Fig. A1(a), was achieved by integrating the two-dimensional diffusion equation

$$\frac{\partial P_{vap}}{\partial t} = D_{vap} \nabla^2 P_{vap} \quad (\text{A1})$$

where D_{vap} is the diffusion coefficient of water vapor through air, which is computed by (see Air-Diffusion Coefficients of Gases in Excess of Air),

$$D_{vap} = D_{vap}^o \left(\frac{P_{amb}}{1 \text{ atm}} \right)^{-1} \left(\frac{T_{amb}}{273 \text{ K}} \right)^{m_D} \quad (\text{A2})$$

Equation A1 is solved subject to Neumann boundary conditions that represent depletion of water vapor in the layer adjacent to the crystal surface due to crystal growth. This rate of depletion is given by

$$-g_{ice} \times \rho_{ice} \times \frac{RT}{M_{H_2O}} \quad (\text{A3})$$

where

- g_{ice} , the specified growth rate of the ice surface;
- ρ_{ice} , the mass density of ice; and
- M_{H_2O} , the molar mass of water

Dirichlet conditions representing the far-field vapor concentration ($P_{vap,f}$), are imposed at the outside boundary of the simulation space. Integration over time was performed using Euler's method, parameters for which are given in Table A1.

Table A1. Parameters for simulation of the vapor field around a growing, square-shaped ice crystal

Simulation space dimensions	$X = Y = \pm 500 \mu m$
Time step for integration	$dt = 5 \times 10^{-5} \mu s$
Time interval for integration	$t_{max} = 2 \mu s$
Spatial discretization	$dx = dy = 2.8 \mu m$
Diffusion coefficient at $T_{amb} = 273 K, P_{amb} = 1 atm$	$D_{vap}^o = 21.9 \mu m^2/\mu s$
Ambient temperature	$T_{amb} = 240 K$
Ambient pressure	$P_{amb} = 68.6 Pa$
Diffusion Temperature-correction exponent	$m_D = 1.86$
Diffusion coefficient under ambient conditions	$D_{vap} = 3.49 \times 10^4 \mu m^2/\mu s$
Far-field water vapor partial pressure	$P_{vap,f} = 30 Pa$
Far-field water vapor supersaturation	$x_f = 1000 \mu m$
Far-field distance from the origin	$\sigma_I = 0.25$
Mass density of ice	$d_{ice} = 0.9 g/cm^2$
Growth rate of ice surface	$g_{ice,s} = 2 \mu m/s$

The resulting vapor concentration contours shown in Fig. A1(a) are seen to decrease with proximity to the crystal, as expected since the growing crystal is drawing water vapor out of the surrounding air. This reduction is greater at facet center compared to facet corners, in a roughly parabolic fashion, as shown in the profile in Fig. A1(b).

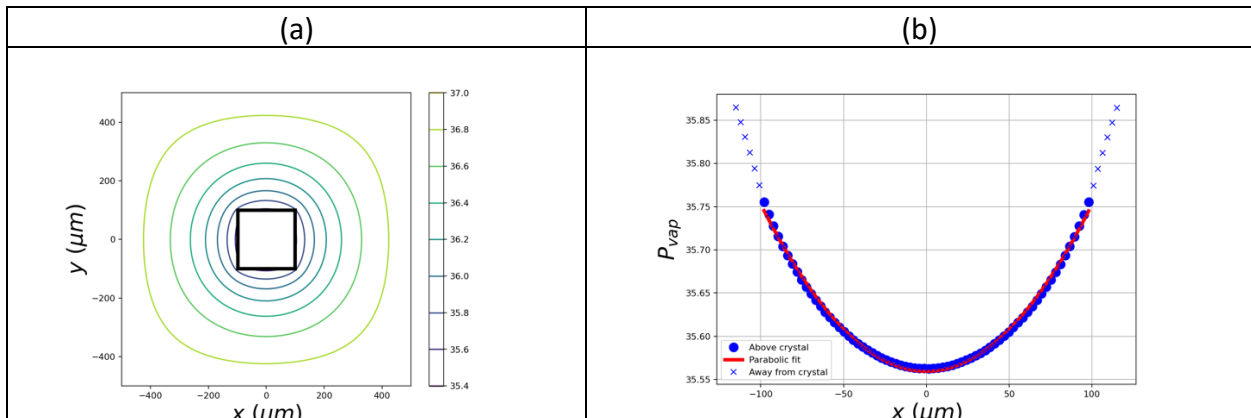


Figure A1. (a) Simulation of vapor partial pressures, $P_{vap}(x, y)$, in units Pa , around a growing ice crystal. The black-outlined box at the center indicates the surface of the crystal, in this case spanning $\pm 100 \mu m$. Contours outside the crystal show values of P_{vap} at steady state. Dirichlet conditions fix a partial pressure of $P_{H_2O,f}$ at the far-field distance of $\pm L = 500 \mu m$, while Neumann conditions representing ice growth are imposed at $\pm L = 100 \mu m$ (see text). (b) P_{vap} along the surface of the crystal.

Supersaturation values are computed from these values using

$$\sigma_I = \frac{P_{vap} - P_{vap}^{eq}(T)}{P_{vap}^{eq}(T)} \quad (\text{A4})$$

Appendix 2 – ESEM/GNBF retrieval

Here is a summary of key equations and constraints in the ESEM/GNBF retrieval ...

Appendix 3 – Numerical considerations

Python, accelerated with NumPy. Code and data are available on Github.

References:

- Anon. n.d. "Air - Diffusion Coefficients of Gases in Excess of Air." Retrieved February 4, 2024 (https://www.engineeringtoolbox.com/air-diffusion-coefficient-gas-mixture-temperature-d_2010.html).
- Benet, Jorge, Pablo Llombart, Eduardo Sanz, and Luis G. MacDowell. 2019. "Structure and Fluctuations of the Premelted Liquid Film of Ice at the Triple Point." *Molecular Physics* 117(20):2846–64. doi: 10.1080/00268976.2019.1583388.
- Butterfield, Nicholas, Penny M. Rowe, Emily Stewart, David Roesel, and Steven Neshyba. 2017. "Quantitative Three-Dimensional Ice Roughness from Scanning Electron Microscopy." *Journal of Geophysical Research: Atmospheres* 122(5):3023–41. doi: 10.1002/2016JD026094.
- Harrington, Jerry Y., and Gwenore F. Pokrifka. 2021. "Approximate Models for Lateral Growth on Ice Crystal Surfaces during Vapor Depositional Growth." *Journal of the Atmospheric Sciences* 78(3):967–81. doi: 10.1175/JAS-D-20-0228.1.
- Järvinen, Emma, Bastiaan van Diedenhoven, Nathan Magee, Steven Neshyba, Martin Schnaiter, Guanglang Xu, Olivier Jourdan, David Delene, Fritz Waitz, Simone Lolli, and Seiji Kato. 2023. "Ice Crystal Complexity and Link to the Cirrus Cloud Radiative Effect." Pp. 47–85 in *Clouds and Their Climatic Impacts*. American Geophysical Union (AGU).
- Jayaprakash, C., W. F. Saam, and S. Teitel. 1983. "Roughening and Facet Formation in Crystals." *Physical Review Letters* 50(25):2017–20. doi: 10.1103/PhysRevLett.50.2017.
- Kuroda, T., and R. Lacmann. 1982. "Growth Kinetics of Ice from the Vapour Phase and Its Growth Forms." *Journal of Crystal Growth* 56(1):189–205. doi: 10.1016/0022-0248(82)90028-8.
- Llombart, Pablo, E. Noya, and Luis MacDowell. 2020. "Surface Phase Transitions and Crystal Habits of Ice in the Atmosphere." *Science Advances* 6:eaay9322. doi: 10.1126/sciadv.aay9322.

- Magee, N. B., A. Miller, M. Amaral, and A. Cumiskey. 2014. "Mesoscopic Surface Roughness of Ice Crystals Pervasive across a Wide Range of Ice Crystal Conditions." *Atmospheric Chemistry and Physics* 14(22):12357–71. doi: 10.5194/acp-14-12357-2014.
- Magee, Nathan, Katie Boaggio, Samantha Staskiewicz, Aaron Lynn, Xuanyi Zhao, Nicholas Tusay, Terance Schuh, Manisha Bandamede, Lucas Bancroft, David Connelly, Kevin Hurler, Bryan Miner, and Elissa Khoudary. 2021. "Captured Cirrus Ice Particles in High Definition." *Atmospheric Chemistry and Physics* 21(9):7171–85. doi: 10.5194/acp-21-7171-2021.
- Murata, Ken-ichiro, Ken Nagashima, and Gen Sazaki. 2019. "How Do Ice Crystals Grow inside Quasiliquid Layers?" *Physical Review Letters* 122(2):026102. doi: 10.1103/PhysRevLett.122.026102.
- Neshyba, Steven, Jonathan Adams, Kelsey Reed, Penny M. Rowe, and Ivan Gladich. 2016. "A Quasi-Liquid Mediated Continuum Model of Faceted Ice Dynamics." *Journal of Geophysical Research: Atmospheres* 121(23):14,035–14,055. doi: <https://doi.org/10.1002/2016JD025458>.
- Neshyba, Steven, Erin Nugent, Martina Roeselová, and Pavel Jungwirth. 2009. "Molecular Dynamics Study of Ice–Vapor Interactions via the Quasi-Liquid Layer." *The Journal of Physical Chemistry C* 113(11):4597–4604. doi: 10.1021/jp810589a.
- Pfalzgraff, W. C., R. M. Hulscher, and S. P. Neshyba. 2010. "Scanning Electron Microscopy and Molecular Dynamics of Surfaces of Growing and Ablating Hexagonal Ice Crystals." *Atmos. Chem. Phys.* 10(6):2927–35. doi: 10.5194/acp-10-2927-2010.
- Price, William S., Hiroyuki Ide, and Yoji Arata. 1999. "Self-Diffusion of Supercooled Water to 238 K Using PGSE NMR Diffusion Measurements." *The Journal of Physical Chemistry A* 103(4):448–50. doi: 10.1021/jp9839044.
- Shohet, Gil, Jacob Price, Jeffrey Haack, Mathieu Marciante, and Michael S. Murillo. 2020. "Heterogeneous Multiscale Method for High Energy-Density Matter: Connecting Kinetic Theory and Molecular Dynamics." *Journal of Computational Physics: X* 8:100070. doi: 10.1016/j.jcpx.2020.100070.
- Walden, Von P., Stephen G. Warren, and Elizabeth Tuttle. 2003. "Atmospheric Ice Crystals over the Antarctic Plateau in Winter." *Journal of Applied Meteorology and Climatology* 42(10):1391–1405. doi: 10.1175/1520-0450(2003)042<1391:AICOTA>2.0.CO;2.
- Zimmermann, Frank, Martin Ebert, Annette Worringen, Lothar Schütz, and Stephan Weinbruch. 2007. "Environmental Scanning Electron Microscopy (ESEM) as a New Technique to Determine the Ice Nucleation Capability of Individual Atmospheric Aerosol Particles." *Atmospheric Environment* 41(37):8219–27. doi: 10.1016/j.atmosenv.2007.06.023.

Other notes ...

 Luis G. MacDowell Mar 9, 2020
sent you the full-text you requested

Dear Steven, thanks for your interest. Note Eq.8 of this paper, with a cosine term that resembles your ideas on Nesyba et al 2016. We found a way to work out the dynamics employed in Eq.8 and that yields a set of coupled equation...

Structure and fluctuations of the premelted liquid film of ice at the triple point

Preprint Mar 2020

Jorge Benet · Pablo Liombart · Eduardo Sanz · Luis G. MacDowell

[Download full-text](#) [Recommend preprint](#) [Say thanks](#)